Editors' Suggestion

Spin and Charge Interconversion in Dirac-Semimetal Thin Films

Wilson Yanez,[1] Yongxi Ou,[1] Run Xiao,[1] Jahyun Koo,[2] Jacob T. Held,[3] Supriya Ghosh,[3] Jeffrey Rable,[1] Timothy Pillsbury,[1] Enrique González Delgado,[4] Kezhou Yang,[5] Juan Chamorro,[6] Alexander J. Grutter,[7] Patrick Quarterman,[7] Anthony Richardella,[1] Abhronil Sengupta,[8] Tyrel McQueen,[6] Julie A. Borchers,[7] K. Andre Mkhoyan,[3] Binghai Yan,[2] and Nitin Samarth[1,*]

[1] *Department of Physics, Pennsylvania State University, University Park, Pennsylvania 16802, USA*
[2] *Department of Condensed Matter Physics, Weizmann Institute of Science, Rehovot 7610001, Israel*
[3] *Department of Chemical Engineering and Materials Science, University of Minnesota, Minneapolis, Minnesota 55455, USA*
[4] *Department of Physics and Electronics, Humacao Campus of the University of Puerto Rico, 100 Tejas Avenue, Humacao 00791-4300, Puerto Rico*
[5] *Department of Materials Science and Engineering, Pennsylvania State University, University Park, Pennsylvania 16802, USA*
[6] *Department of Chemistry, Johns Hopkins University, Baltimore, Maryland, USA*
[7] *NIST Center for Neutron Research, National Institute of Standards and Technology, Gaithersburg, Maryland 20899, USA*
[8] *School of Electrical Engineering and Computer Science, Pennsylvania State University, University Park, Pennsylvania 16802, USA*

(Received 3 March 2021; revised 23 September 2021; accepted 28 September 2021; published 16 November 2021)

We use spin torque ferromagnetic resonance and ferromagnetic-resonance-driven spin pumping to detect spin-charge interconversion at room temperature in heterostructure devices that interface an archetypal Dirac semimetal, Cd_3As_2, with a metallic ferromagnet, $Ni_{0.80}Fe_{0.20}$ (permalloy). Angle-resolved photoemission directly reveals the Dirac-semimetal nature of the samples prior to device fabrication and high-resolution transmission electron microscopy is used to characterize the crystalline structure and the relevant heterointerfaces. We find that the spin-charge interconversion efficiency in Cd_3As_2/permalloy heterostructures is comparable to that in heavy metals and that it is enhanced by the presence of an interfacial oxide. Spin torque ferromagnetic resonance measurements reveal an in-plane spin polarization regardless of an oxidized or pristine interface. We discuss the underlying mechanisms for spin-charge interconversion by comparing our results with first principles calculations and conclude that extrinsic mechanisms dominate the observed phenomena. Our results indicate a need for caution in interpretations of spin-transport and spin-charge conversion experiments in Cd_3As_2 devices that seek to invoke the role of topological Dirac and Fermi arc states.

DOI: 10.1103/PhysRevApplied.16.054031

I. INTRODUCTION

Spin-to-charge conversion and its Onsager reciprocal charge-to-spin conversion have been studied extensively in several materials with either strong spin-orbit coupling [such as heavy metals (HMs)] or with spin momentum "locking" (as in the surface states of topological insulators) [1–12]. The latter class of materials motivated the emergence of "topological spintronics," broadly aimed at exploiting the strong spin-momentum correlation in helical topological states for spintronic devices. Theoretical studies provide strong motivation for extending such studies to topological semimetals. For example, in Weyl semimetals, calculations predict a large spin Hall conductivity (SHC), the Rashba-Edelstein effect, and efficient spin-to-charge conversion in magnetic Weyl semimetal-normal metal heterostructures [13–15]. Recent experiments have reported current-induced spin-orbit torques in the Weyl semimetal WTe_2 with efficiencies comparable to HMs [16,17]. In addition, field-free current-induced magnetization switching has been demonstrated at room temperature in WTe_2/ferromagnet heterostructures with current densities lower than HMs and topological insulators [18]. This context motivates the exploration of spin-charge interconversion in a different class of topological semimetals of contemporary interest, the Dirac semimetal (DSM), where only a few studies of spin transport have been reported

*nsamarth@psu.edu

 © 2021 American Physical Society

[19–22]. We might anticipate that the interplay between a bulk three-dimensional linear dispersion with nontrivial topology and the spin polarization of surface states could give rise to efficient spin-charge interconversion and, thus, elicit interest for spintronics [14,18,23–25]. Unlike the intuitive appeal of spin-momentum locked states in topological insulators and Weyl semimetals for topological spintronics, however, the spin degeneracy inherent in the topological band structure of a DSM raises a fundamental question that has not yet been answered: what is the SHC of a DSM and could it be relevant for spintronics?

In this paper, we report measurements of spin-charge interconversion at room temperature in bilayers of the archetypal DSM Cd_3As_2 and a conventional metallic ferromagnet, $Ni_{0.80}Fe_{0.20}$ (permalloy, Py) via spin torque ferromagnetic resonance (ST-FMR) and ferromagnetic resonance driven spin pumping (SP). We also compare our experimental results with first principles calculations of the SHC in Cd_3As_2. In bilayers with an imperfect (oxidized) interface, we find a SHC that is much larger than predicted by theory at the estimated chemical potential and comparable to that of HMs. We attribute the dominant contributions to extrinsic effects. Measurements of bilayers with a clean interface show a smaller SHC, consistent with our theoretical predictions for intrinsic contributions to spin-charge interconversion. These results suggest caution about the interpretation of experiments that attribute observations of spin transport to the topological states of Cd_3As_2 [19,20,22].

II. SAMPLE SYNTHESIS AND CHARACTERIZATION

We first discuss the synthesis, as well as structural and interfacial characterization, of Cd_3As_2/Py heterostructures. We used molecular beam epitaxy (MBE) to grow Cd_3As_2 thin films under ultrahigh vacuum conditions (pressure $P < 10^{-7}$ Pa) in a Veeco 930 system. We first grew an intrinsic, relaxed GaSb (111) buffer layer (100 nm thick) on a semi-insulating GaAs(111)B substrate using elemental Ga (5N) and Sb (5N) source materials evaporated from standard effusion cells. The growth conditions used were standard for the III–V semiconductor. The Cd_3As_2 layer was then deposited at a substrate temperature $T_s \sim 200\,^{\circ}$C. For most of the samples discussed in this paper, the source materials are elemental Cd (5N purity) and As (5N purity) evaporated from conventional effusion cells; the beam equivalent flux ratio of Cd:As was 3:2. Some samples were also grown by evaporating a compound Cd_3As_2 source, also from an effusion cell. Typical growth rates were 0.5 nm/min. During MBE growth, we obtain an unreconstructed streaky reflection high-energy electron diffraction (RHEED) pattern [Figs. 1(a) and 1(b)] which shows the expected C_3 symmetry of the Cd_3As_2 crystal. X-ray diffraction [Fig. 1(c)] shows peaks corresponding to Cd_3As_2 grown in the ⟨112⟩ orientation as well as the peaks of the GaSb (111) buffer layer and the GaAs (111) substrate. Typical double crystal rocking curves for diffraction peaks from Cd_3As_2 have widths of ∼0.11°. Atomic force microscopy (AFM) [Fig. 1(d)] shows large domains (500 nm lateral islands) with 0.5 nm high steps. These are all signatures of epitaxial growth of reasonable quality Cd_3As_2 thin films, similar to those reported in prior literature [26].

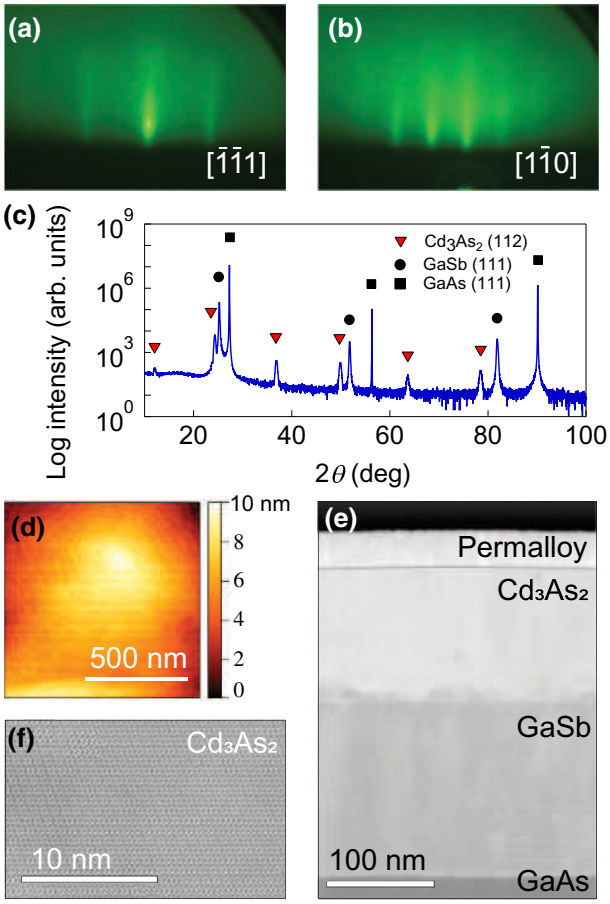

FIG. 1. RHEED pattern of the Cd_3As_2 film along the (a) [1̄1̄1] and (b) [11̄0] crystal directions. (c) X-ray diffraction 2θ scan of Cd_3As_2 films. (d) AFM image of the Cd_3As_2 surface. High-angle annular dark-field STEM image showing the different layers in (e) a complete device stack and (f) just the Cd_3As_2 layer.

The measurement of spin-charge interconversion in Cd_3As_2 requires the synthesis of heterostructures that interface a well-characterized ferromagnet with the DSM. To this end, we transferred the MBE-grown Cd_3As_2 films to a different vacuum chamber for the deposition of Py thin films using an e-beam evaporator. Most of the spin-charge interconversion data are taken on samples that involved brief (10–15 min) exposure of the Cd_3As_2 film to ambient atmosphere before the subsequent deposition of a Py thin

film, followed by 1–3 nm of either Ta or Al as a capping layer to prevent oxidation. Although technical limitations currently constrain our capability for the routine deposition of Py on Cd_3As_2 without breaking vacuum, we also include spin-charge interconversion data on a sample grown with a pristine interface.

We further characterized the Cd_3As_2/Py heterostructures using atomic-resolution high-angle annular dark-field (HAADF) scanning transmission electron microscopy (STEM). An example of such data for a heterostructure with brief ambient exposure between MBE growth of Cd_3As_2 and Py deposition is shown in Figs. 1(e) and 1(f): the former reveals coherent growth of the entire heterostructure, albeit with the presence of a 1 nm cadmium oxide layer at the Cd_3As_2/Py interface as confirmed by energy dispersive X-ray (EDX) spectroscopy. More detailed STEM and EDX characterization is available in Appendix D. As proximity-induced magnetism at the interface between the DSM and metallic ferromagnet might play a role in spin-charge interconversion, we also used polarized neutron reflectometry (PNR) measurements to characterize the magnetic behavior at the Cd_3As_2/Py interface. We do not observe any evidence for proximity-induced magnetism in the Cd_3As_2 layer (see Appendix E).

To confirm the presence of a DSM state in the MBE-grown Cd_3As_2 thin films, we carried out angle-resolved photoemission spectroscopy (ARPES) measurements on a few samples that were transferred from the MBE chamber to a local ARPES measurement chamber while maintaining a vacuum environment with pressure $1.3 \lesssim \mu$Pa. We used the 21 eV helium Iα spectral line from a helium plasma lamp isolated via a monochromator as the photon source. The emitted photoelectrons were imaged by a ScientaOmicron DA 30L analyzer with a maximum spectral resolution of 6 meV. Figures 2(a) and 2(b) show ARPES measurements from a Cd_3As_2 thin film at room temperature. The spectra are similar to those reported in the prior literature on cleaved bulk crystals of Cd_3As_2 [27–29]. The data show the characteristic linear dispersion in the vicinity of the charge neutral point expected for a DSM. The ARPES data also indicate that the charge neutral point is located 0.2 eV below the chemical potential. This is consistent among several samples with different thicknesses. It is important to note that ARPES cannot probe the surface state of these Cd_3As_2 films once the surface has been capped with Py. Thus, we do not have any direct knowledge of the nature of the electronic states at the Cd_3As_2/Py interface. This is a limitation in all the published studies on topological spintronics thus far.

We carried out electrical magneto-transport measurements on uncapped and As-capped Cd_3As_2 thin films at room temperature, revealing a Hall resistance with nonlinear dependence on magnetic field, indicative of coexisting electron and hole type of carriers as expected for a

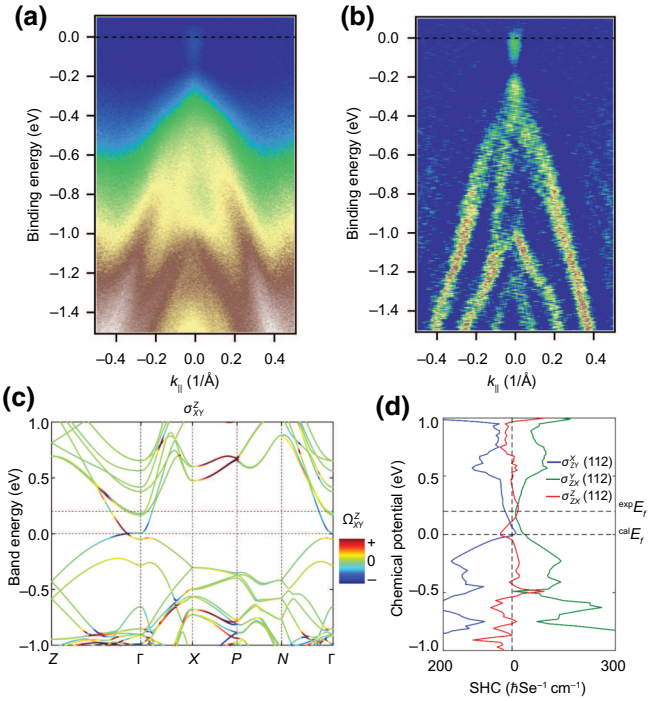

FIG. 2. (a) Electronic band structure of Cd_3As_2 thin films obtained by ARPES. The measurements are taken at $T = 300$ K along the K–Γ–K direction, projected on the (112) surface. (b) Second derivative of the spectrum shown in (a). (c) Calculated band structure and spin Hall conductivity (SHC) of bulk Cd_3As_2 The color in the band structure shows the spin Berry curvature (Ω^z_{xy}) with z along the [001] direction. (d) Three independent components of SHC with z along the [112] direction as a function of chemical potential.

chemical potential close to the charge neutral point [30–32]. In the low field limit (the range needed for ST-FMR and SP experiments), the electrical transport is mainly electron type with a carrier density and mobility of around $n = 10^{18} - 10^{19}$ cm^{-3} and $\mu = 4000 - 6000$ cm^2 V^{-1} s^{-1} measured at different temperatures and thicknesses.

III. THEORETICAL CALCULATION OF SPIN HALL CONDUCTIVITY

To obtain a theoretical understanding of the spin-charge interconversion in Cd_3As_2, we performed density-functional theory (DFT) calculations in the framework of the generalized gradient approximation [33] with a full-potential local-orbital (FPLO) minimum-basis code [34]. Spin-orbit coupling was included. The crystal structure of Cd_3As_2 belongs to space group $I4_1/acd$ (No. 142) and has inversion symmetry [35]. From DFT calculations, we projected the Bloch wave function into atomic-like Wannier functions of Cd-5s orbital and As-4p orbitals. Then we build an accurate tight-binding Hamiltonian ($\hat{H}$) to calculate the intrinsic SHC components [Figs. 2(c) and

2(d)] [36]. Full details of the calculation are given in Appendix A.

In addition, our calculation reveals an out-of-plane spin polarization in the spin current generated by the intrinsic SHC $\sigma_{zx}^{z} = 16(\hbar/e)$ S cm^{-1}, where spin current direction z refers to the [112] direction. The nonzero σ_{zx}^{z} is induced by the symmetry breaking along the [112] axis. If the intrinsic SHE prevails under certain experimental conditions, we expect that the out-of-plane polarization may play a significant role in the spin-orbit torque. We also find that the SHC has several local maxima around the charge neutral point. This could tentatively explain the variation of the spin-charge interconversion efficiency with changes of chemical potential seen in Refs. [19,20]. It also offers an opportunity to enhance the intrinsic SHC in Cd_3As_2 thin films via chemical doping or electrostatic gating.

IV. SPIN TORQUE FERROMAGNETIC RESONANCE

We now discuss the spin-charge interconversion in Cd_3As_2/Py bilayers. We have measured a total of 13 devices (5 using ST-FMR and 8 using SP) all showing the interconversion phenomenon. In all these devices except for one, the interface between Cd_3As_2 and Py has some oxidation due to brief ambient exposure. In ST-FMR experiments, we apply a radio frequency (rf) charge current in devices with lateral device dimensions 50 μm $\times$ 10 μm patterned from bilayers of 8 nm to 80 nm thick Cd_3As_2 and 4 nm to 6 nm thick Py in the presence of an in-plane external magnetic field. This process excites the magnetization dynamics of the ferromagnetic layer by means of Oersted field and spin current at the interface. The latter results from the rf charge current creating a flow of angular momentum perpendicular to the interface (charge-to-spin conversion) in the DSM [Fig 3(a)]. The magnetization dynamics are then probed using the anisotropic magnetoresistance of the ferromagnetic layer which, along with the rf current, produces a DC mixing voltage ($V_{\rm mix}$) in the device. The in-plane and out-of-plane torques can then be extracted by fitting the $V_{\rm mix}$ with a symmetric and antisymmetric Lorentzian function:

$$V_{\rm mix} = \frac{S\Delta^2_{Cd_3As_2} + A\Delta_{Cd_3As_2}(H - H_{\rm Res})}{\Delta^2_{Cd_3As_2} + (H - H_{\rm Res})^2}. \qquad (1)$$

Here, $\Delta_{Cd_3As_2}$ is the line width of the absorption spectrum, H is the applied external field, $H_{\rm Res}$ is the field at which we see the resonance, and $S(A)$ is the magnitude of the symmetric (antisymmetric) component. The frequency dependence of the absorption spectrum is well understood for thin films using the Kittel equation $f = (\gamma/2\pi)\sqrt{H_{\rm Res}(H_{\rm Res} + M_{\rm Eff})}$. This can be fitted to our data using the known gyromagnetic ratio of the electron (γ), giving effective magnetization values of around

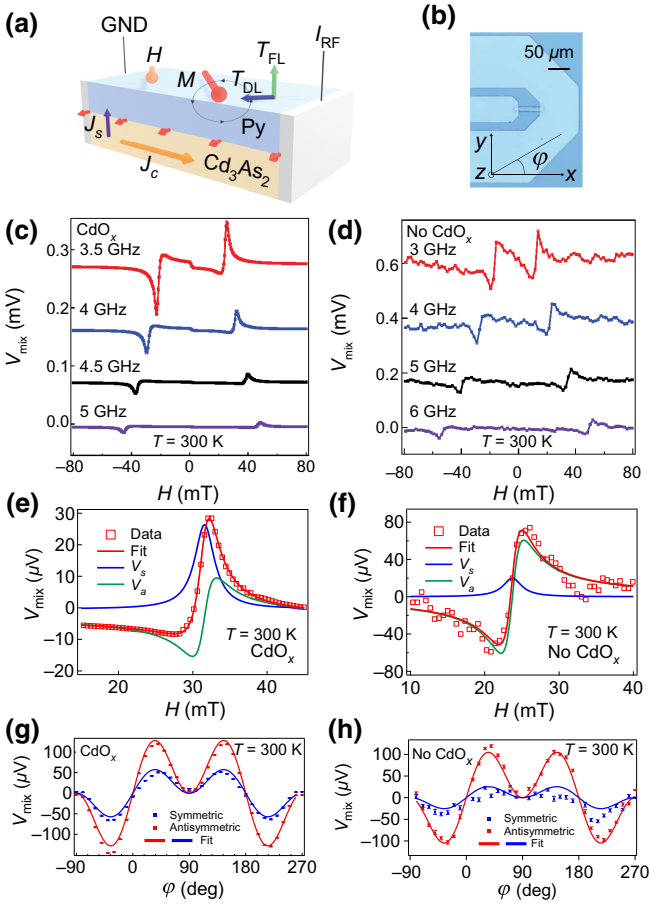

FIG. 3. (a) Illustration of charge-to-spin conversion due to ST-FMR. (b) Optical microscope image of the ST-FMR device. ST-FMR mixing voltage signal measured in (c) a Py(4 nm)/Cd_3As_2(12 nm) heterostructure with CdO_x and (d) in an *in vacuo* grown Py(5 nm)/Cd_3As_2(8 nm) heterostructure without CdO_x. We used a microwave power of 20 dBm and swept the magnetic field at different frequencies (data have been offset in both cases for clarity). (e),(f) ST-FMR spectra of the same devices shown in (c),(d), respectively, at 4 GHz showing the measured data and the fit needed to extract the symmetric (S) and antisymmetric (A) components of the torque. Angle dependence of the symmetric and antisymmetric components of the torque fitted with $\sin(\phi)\cos(\phi)^2$ for (g) the sample with CdO_x and (h) for the completely *in vacuo* grown sample.

$M_{\rm Eff} = 560$ kA/m to 640 kA/m which is similar to values reported by FMR studies in Py films [37].

In addition, we use the ratio of the symmetric and antisymmetric components to extract the spin torque efficiency defined as the ratio of the rf spin current (J_s) generated in the device and the charge current (J_c) applied by an external source [38,39]:

$$\xi = \frac{2e}{\hbar}\frac{J_s}{J_c} = \frac{S}{A}\frac{e\mu_0 M_S t_{Cd_3As_2} t_{\rm NiFe}}{\hbar}\left[1 + \left(\frac{M_{\rm Eff}}{H_{\rm Res}}\right)\right]^{1/2}. \qquad (2)$$

Here, e is the charge of the electron, $\hbar$ is the reduced Planck constant, μ_0 is the permeability of free space, $M_S = 560$ kA/m is the saturation magnetization of Py (measured in a Quantum Design superconducting quantum interference device magnetometer), $t_{Cd_3As_2}$ is the thickness of the Cd_3As_2 layer, and t_{NiFe} is the thickness of the ferromagnet. To address the possibility of a three-dimensional spin polarization, we have measured the ST-FMR spectra while changing the angle (ϕ) between the current and the magnetic field direction with the axes shown in Fig. 3(b).

Figure 3(c) shows the mixing voltage of a device with the CdO_x interfacial layer, measured at different frequencies ranging from 3.5 to 5 GHz. The spin torque efficiency ξ is extracted from the measured signal by separating it into a symmetric and an antisymmetric Lorentzian component, as shown in Fig. 3(e). If we assume that the spin current has a bulk origin in the samples with the CdO_x interfacial layer, we obtain a spin torque efficiency $\xi = 0.27$ (0.22) with 4 (6) nm of Py, comparable to values in HM. This provided a lower bound on the spin Hall angle due to the less than ideal spin transparency [39]. The spin torque efficiency can then be combined with the Cd_3As_2 conductivity ($\sigma_{xx} \approx 1250$ S cm^{-1}) to extract the SHC:

$$\sigma_{SH} = \frac{\hbar}{2e}\theta_{SH}\sigma_{xx} \gtrsim 140\,\frac{\hbar}{e}\ \mathrm{S\,cm^{-1}}. \tag{3}$$

As a first step to better understand the intrinsic contributions to the SHC of Cd_3As_2, we have studied ST-FMR in devices fabricated from Cd_3As_2/Py bilayers grown using a full *in vacuo* transfer procedure [Fig. 3(d)]. STEM characterization of such a sample showed a clean Cd_3As_2/Py interface (see Appendix D). The ST-FMR signal is, however, weaker than in the devices fabricated from bilayers with an oxidized interface. Analysis of the ST-FMR data show that the spin torque efficiency ($\xi = 0.10$) and the SHC ($\sigma_{SH} = 63(\hbar/e)$ S cm^{-1}) are closer to the intrinsic theoretical value, indicating that the interfacial cadmium oxide layer enhances the SHC. We also note that the symmetric component of the torque in both systems shows the same sign as in Pt and opposite to that in W, in agreement with the theoretical prediction of a positive SHC. In both the samples with an oxidized interface and pristine interface, the variation of the ST-FMR as a function of in-plane field angle [Figs. 3(e) and 3(f)] shows the expected symmetry of the in-plane and out-of-plane torques. This behavior is consistent with contributions expected from the bulk spin Hall effect, the Oersted field, or the Rashba-Edelstein effect [10,38,40,41]. The data can be reasonably fit with a $\sin(\phi)\cos(\phi)^2$ function, indicating the absence of spin polarization in the out-of-plane or current flow directions in both systems (see Appendices B and D).

V. SPIN PUMPING

To complement the ST-FMR measurements of spin-charge interconversion, we also carried out SP measurements on Cd_3As_2/Py heterostructures. All the data presented here were measured using samples with a partially oxidized interface. In these experiments, we placed the Cd_3As_2/Py heterostructure in a grounded microstrip transmission line. We studied the FMR of the Py ferromagnet by applying a fixed rf signal in the transmission line while sweeping an external magnetic field [Fig. 4(a)] [1,2,8,42]. The external magnetic field excites the dynamics of the ferromagnet, generating precession of its magnetization which can then be measured as a change in the power absorbed under resonance conditions [Fig. 4(c)] [1,8,12]. The frequency dependence of this FMR phenomenon is again characterized by the Kittel equation. As we performed the FMR experiment, we simultaneously measured the voltage generated in the Cd_3As_2 film under resonance conditions [Fig. 4(b)]. This signal can be decomposed into two contributions. The dominant contribution is linear in power [Fig. 4(d)] and changes sign with magnetic field direction (V_{SP}). The secondary contribution is less than 1.5 μV and does not change sign under field reversal (see Appendix C) [43]. The behavior of V_{SP}, which we attribute to spin to charge conversion due to spin pumping from the ferromagnet is similar to the inverse spin Hall effect (ISHE) in HMs and the inverse Rashba-Edelstein effect (IREE) in topological insulators and two-dimensional electron systems in which an electric field ($\vec{E}$) is generated in a direction perpendicular to the spin current (J_s) and its spin polarization (σ), i.e., $\vec{E} \propto \vec{J}_s \times \vec{\sigma}$ [1,8,12,37]. Again, the sign of the voltage signal matched that of Pt, consistent with our ST-FMR and theoretical results.

We have measured SP in 8 heterostructures with Cd_3As_2 film thickness ranging from 12 to 200 nm (measured by STEM and X-ray reflectivity) and a Py thickness of 30 nm. In addition, as a control experiment, we performed the same SP measurement in a sample with just Py and the GaSb buffer layer; we did not detect a voltage signal under resonance conditions. Thus, we are sure that the spin-to-charge conversion is due to the presence of the Cd_3As_2 layer. We also use the broadening of the linewidth of the absorption spectra in the Cd_3As_2 samples ($\Delta H_{Cd_3As_2}$) and the GaSb samples (ΔH_{GaSb}) to compare the spin mixing conductance ($g_{\uparrow\downarrow}$) in the two cases [1,8,44]:

$$g_{\uparrow\downarrow} = \frac{2\pi\sqrt{3}M_S\gamma t_{NiFe}}{g\mu_B\omega}(\Delta H_{Cd_3As_2} - \Delta H_{GaSb}). \tag{4}$$

Here, g is the Landé factor, μ_B is the Bohr magneton, and ω is the resonance frequency of our samples (ranging between 5 and 12 mm). We obtain a spin mixing conductance in the range between 1.0×10^{18} and 3.5×10^{18} m^{-2}.

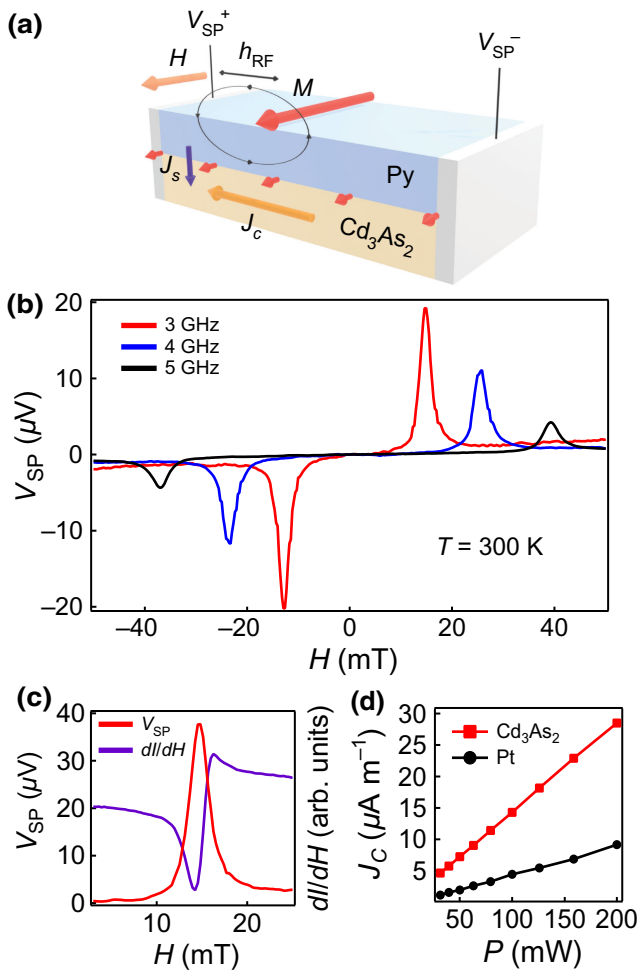

FIG. 4. (a) Illustration of spin-to-charge conversion due to SP. (b) Voltage signal measured in the Cd_3As_2(40 nm)/Py(30 nm) heterostructure at room temperature with an applied microwave power of 20 dBm. (c) SP voltage signal (V_{SP}) and FMR absorption spectra (dI/dH) measured at 3 GHz and 23 dBm. (d) Charge current (J_c) as a function of power for Cd_3As_2(40 nm)/Py(30 nm) and Py(30 nm)/Pt(20 nm) heterostructures showing linear behavior.

The difference in spin mixing conductance amongst samples might be due to variations in the Py/Cd_3As_2 interface during fabrication. We can further compute the spin current pumped into the Cd_3As_2 layer using the equation [1,8]

$$J_S = \frac{2e}{\hbar}\frac{g_{\uparrow\downarrow}h_{RF}^2\hbar\omega^2\left[\gamma 4\pi M_S + \sqrt{(\gamma 4\pi M_S)^2 + 4\omega^2}\right]}{2\pi(\Delta H_{Cd_3As_2})^2\left[(\gamma 4\pi M_S)^2 + 4\omega^2\right]}. \quad (5)$$

Here, h_{RF} is the magnetic field generated by the transmission line which has been calibrated using the ISHE of Pt and the IREE of Bi_2Se_3. We obtain values of J_s that range between 0.5×10^4 to 3.4×10^4 A m^{-2}.

Finally, we compute the efficiency of the spin-to-charge conversion by calculating the charge current (J_c) generated in the film by normalizing the measured voltage signal by the sample width (w) and its resistance (R). We obtain values that range from 2.6×10^{-7} to 7.0×10^{-6} A m^{-1}. The interconversion is more efficient than the Py(30 nm)/Pt(20 nm) control sample which has $g_{\uparrow\downarrow} = 2.7 \times 10^{18}$ m^{-2}, $J_s = 2.6 \times 10^4$ A m^{-2}, and $J_c = 9.16 \times 10^{-6}$ A m^{-1}. Since DSMs can have both (topological and trivial) surface and bulk states [23], we tentatively describe the efficiency of the conversion in terms of bulk spin Hall angle (θ_{SH}) with spin diffusion length (λ_{SD}) and surface IREE with effective length (λ_{IREE}) [1,8,9].

$$J_c = \frac{V_{SP}}{wR} = -\left[\theta_{SH}\lambda_{SD}\tanh\left(\frac{t_{Cd_3As_2}}{2\lambda_{SD}}\right) + \lambda_{IREE}\right]J_S. \quad (6)$$

Large variations in sample fabrication (differences in roughness, carrier density, and the presence of CdO_x at the Py/Cd_3As_2 interface) prevent reliable fits to equation 6 (see Appendix F). Nevertheless, we can draw some conclusions in limiting cases. If we assume that the spin-charge conversion is governed solely by the two-dimensional Rashba-Edelstsein physics at the interface of the sample, we can approximate $J_c/J_s = \lambda_{IREE}$, yielding values in the range of approximately $0.1 - 1.2$ nm. This spread in values might be due to variations in the interface among samples [45–47]. Instead, if we assume that the spin-charge conversion is dominated by a three-dimensional bulk contribution with a spin diffusion length in Cd_3As_2 that is smaller than the thickness of our thinnest spin pumping samples ($\lambda_{SD} <$ 40 nm), we can approximate $J_c/J_s = \theta_{SH}\lambda_{SD}$. Combined with the spin torque efficiency measured using ST-FMR, this yields $\lambda_{SD} \lesssim 5.5$ nm.

VI. DISCUSSION

We now summarize our experimental findings, discuss them in the context of our theoretical calculations, and compare them with other recent experiments that have attempted to probe spin-charge conversion in Cd_3As_2. In Cd_3As_2/Py bilayers with an oxidized interface, our measurements at room temperature reveal a spin-torque efficiency $\xi \approx 0.22 - 0.27$, a SHC $\sigma_{SH} \gtrsim 140(\hbar/e)$ S cm^{-1}, and spin-charge conversion efficiency $J_C/J_s = \theta_{SH}\lambda_{SD}\tanh(t_{Cd_3As_2}/2\lambda_{SD}) + \lambda_{IREE} \approx 0.1$ nm $- 1.2$ nm. In Cd_3As_2/Py bilayers with a pristine interface, we find $\sigma_{SH} \gtrsim 63(\hbar/e)$ S cm^{-1} and $\xi \approx 0.1$. We note that the spin torque efficiency ξ in both cases is comparable to the reported values of HMs such as β-W and Pt [1,7,12,39]. Finally, the variation of the ST-FMR signal as a function of in-plane field angle indicates that the spin current does not have an out-of-plane polarization. We now discuss these results in light of our theoretical calculations.

The SHE can be theoretically classified into intrinsic and extrinsic contributions. As discussed earlier, the intrinsic SHC of the bulk states, which is determined by the spin Berry curvature in the wave function, can be calculated from the first-principles band structure considering x, y in the (112) crystallographic plane and the spin current along z, as in the experimental setup (see Appendix A). Our calculation shows that the intrinsic SHC is small, close to the charge neutral point and has local maxima either on the electron-doped or hole-doped side. At the chemical potential of the experimental samples, we obtain an intrinsic SHC $\sigma_{zx}^{y} = 10(\hbar/e)$ S cm^{-1}. We note that the surface can also host DSM Fermi arc states that originate from the quantum spin Hall edge states; their contribution to the SHC is equivalent to the intrinsic bulk SHC due to the bulk-boundary correspondence. The predicted value of the SHC is about one order of magnitude smaller than the experimental value of approximately $140(\hbar/e)$ S cm^{-1} measured in samples with an oxidized interface. These observations imply that the SHE in samples with an imperfect interface is dominated by extrinsic effects. Our measurements of samples with a pristine interface reveal a SHC of approximately $63(\hbar/e)$ S cm^{-1}. Although more consistent with theory, this value is still quite large, suggesting that even in the samples with a pristine interface, we cannot rule out an extrinsic mechanism for the experimental observations (for example, the Rashba-Edelstein effect from trivial surface states). In principle, we may be able to identify intrinsic contributions to spin-charge interconversion in Cd_3As_2 by carrying out spin pumping and ST-FMR experiments in electrostatically gated Cd_3As_2 films as a function of chemical potential. However, in our current samples that interface Cd_3As_2 films with a *metallic* FM, this is not physically possible. Our calculations also predict an out-of-plane spin polarization in the spin current due to the intrinsic SHE $\sigma_{zx}^{z} = 16(\hbar/e)$ S cm^{-1}. The nonzero σ_{zx}^{z} is induced by the symmetry breaking along the [112] axis. However, our angle dependent ST-FMR measurements show that the spin is in-plane, perpendicular to the charge and spin current directions, in samples with both oxidized and pristine interfaces.

Thus, our key conclusion is that extrinsic contributions with surface and/or bulk origin dominate the spin-charge interconversion in Cd_3As_2/Py bilayers with both oxidized and pristine interfaces. We draw these conclusions using a concerted set of ST-FMR and spin pumping measurements in thoroughly characterized samples. These observations and conclusions are consistent with studies in other systems showing that oxidation can enhance spin torque phenomena by increasing the bulk spin Hall effect or by producing an interfacial Rashba effect in oxidized metals [48–54]. A rigorous identification of the physical mechanisms responsible for the spin-charge interconversion via these extrinsic mechanisms is beyond the scope of this paper because it requires a detailed microscopic knowledge of the underlying states created by band bending, their spin texture, and the spin-dependent scattering mechanisms.

Finally, we compare our results with other recent studies of spin transport and spin-charge conversion in Cd_3As_2. Measurements of dc spin transport in Cd_3As_2 have been attributed to Fermi arc related physics by performing spin potentiometry in electrostatically gated chemical-vapor-deposition-grown Cd_3As_2 nanowires [19] and nanoplates [20]. Although it is not possible to use ARPES to verify the presence of DSM states (or Fermi arc states) in these nanostructured devices, the gate-dependent transport is consistent with expectations for Dirac states in Cd_3As_2. The measurements show an enhancement of the spin polarization as the chemical potential is tuned close to the charge neutral point. Both these sets of experiments appear to show an in-plane spin polarization, consistent with our experimental measurements but inconsistent with our theoretical predictions for the spin polarization due to the Dirac states in Cd_3As_2. As the devices used in these studies have an oxide over the entire surface of the spin-transport

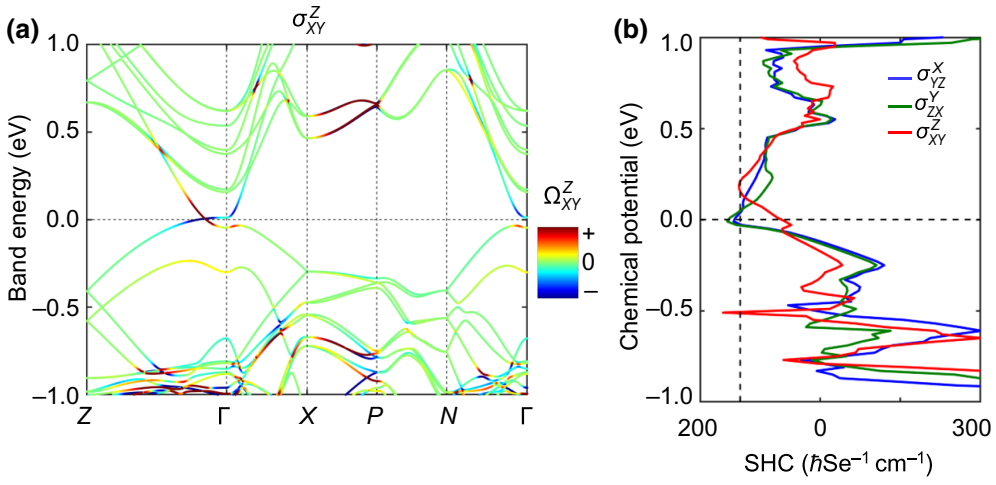

FIG. 5. Band structure, spin Berry curvature, and spin Hall conductivity along the (001) direction. Calculated band structure and spin Hall conductivity of bulk Cd_3As_2. The color in the band structure shows the spin Berry curvature (Ω_{xy}^{z}). The right panel presents three independent values of spin Hall conductivity calculated in the ⟨001⟩ direction as a function of chemical potential.

TABLE I. Calculated spin Hall conductivity of Cd_3As_2 at the charge neutral point. The SHC is in the unit of [S cm^{-1} ($\hbar/e$)].

	σ^x	σ^y	σ^z
Magnetic Laue group 4/mmm z[001]	$\begin{pmatrix} 0 & 0 & 0 \\ 0 & 0 & -\sigma^y_{xz} \\ 0 & -\sigma^y_{zx} & 0 \end{pmatrix}$	$\begin{pmatrix} 0 & 0 & \sigma^y_{xz} \\ 0 & 0 & 0 \\ \sigma^y_{zx} & 0 & 0 \end{pmatrix}$	$\begin{pmatrix} 0 & \sigma^z_{xy} & 0 \\ -\sigma^z_{xy} & 0 & 0 \\ 0 & 0 & 0 \end{pmatrix}$
Calculation z[001]	$\begin{pmatrix} 0 & 0 & 0 \\ 0 & 0 & -1 \\ 0 & 8 & 0 \end{pmatrix}$	$\begin{pmatrix} 0 & 0 & 1 \\ 0 & 0 & 0 \\ -8 & 0 & 0 \end{pmatrix}$	$\begin{pmatrix} 0 & 40 & 0 \\ -40 & 0 & 0 \\ 0 & 0 & 0 \end{pmatrix}$
Calculation z[112]	$\begin{pmatrix} 0 & 0 & 0 \\ 0 & -3 & -6 \\ 0 & 3 & 3 \end{pmatrix}$	$\begin{pmatrix} 0 & -19 & -26 \\ 23 & 0 & 0 \\ 24 & 0 & 0 \end{pmatrix}$	$\begin{pmatrix} 0 & 13 & 19 \\ -8 & 0 & 0 \\ -23 & 0 & 0 \end{pmatrix}$

device (except at the ohmic contacts), it is possible that the extrinsic spin-charge conversion mechanisms identified by our study may also play a role. Indeed, one of these studies [20] insightfully indicated the presence of a Rashba splitting at the interface of Cd_3As_2 and a ferromagnetic metal. In another recent experiment, spin-transport experiments were carried out on devices fashioned from MBE-grown Cd_3As_2 films. The nonlocal Hanle effect was used to deduce very long spin diffusion lengths ($\sim \mu$m at $T = 3$ K) and a nonlocal spin valve effect was observed at room temperature in devices with a spin channel length around 4 μm [22]. Noting that this experiment used MBE-grown Cd_3As_2 thin films with mobility and carrier density similar to those used in our study, we do not have an explanation for the several orders of magnitude discrepancy in the spin diffusion lengths extracted from this dc (or low-frequency) spin-transport experiment and our microwave frequency spin-transport experiments. These discrepancies will only be resolved by carrying out a concerted set of measurements of ST-FMR, spin pumping, spin potentiometry, and nonlocal spin valve measurements in a common set of well-characterized Cd_3As_2 devices.

In summary, we have carried out systematic measurements of spin-charge interconversion in well-characterized films of a topological semimetal, Cd_3As_2, revealing the importance of large extrinsic contributions to the SHC that can arise at an imperfect interface. Even measurements at a pristine interface suggest a contribution that may arise from a trivial (Rashba) surface state. These results show that imperfect interfaces can sometimes be useful for enhancing spin-charge conversion efficiency for practical devices. Our results also raise caution about the interpretation of spin-transport measurements in Cd_3As_2 that attribute observations to surface Fermi arcs. Finally, we provide a theoretical framework that can provide guidance for future studies that seek to differentiate the intrinsic and extrinsic contributions to the spin-transport phenomena in Cd_3As_2.

ACKNOWLEDGMENTS

The principal support for this project was provided by SMART, one of seven centers of nCORE, a Semiconductor Research Corporation program, sponsored by the National Institute of Standards and Technology (NIST). This supported the synthesis and standard characterization of Py/Cd_3As_2 heterostructures as well as spin-charge interconversion measurements (WY, YO, NS) and their characterization using STEM (JH, SG, AM). Additional support for materials synthesis was provided by the Institute for Quantum Matter under DOE EFRC grant DE-SC0019331 (RX, JC, NS, TM). The Penn State Two-Dimensional Crystal Consortium-Materials Innovation Platform (2DCC-MIP) under NSF

TABLE II. Calculated spin Hall conductivity of Cd_3As_2 at the experimental Fermi level (0.2 eV above the charge neutral point). The SHC is in the unit of S cm^{-1} ($\hbar/e$).

	σ^x	σ^y	σ^z
Magnetic Laue group 4/mmm z[001]	$\begin{pmatrix} 0 & 0 & 0 \\ 0 & 0 & -\sigma^y_{xz} \\ 0 & -\sigma^y_{zx} & 0 \end{pmatrix}$	$\begin{pmatrix} 0 & 0 & \sigma^y_{xz} \\ 0 & 0 & 0 \\ \sigma^y_{zx} & 0 & 0 \end{pmatrix}$	$\begin{pmatrix} 0 & \sigma^z_{xy} & 0 \\ -\sigma^z_{xy} & 0 & 0 \\ 0 & 0 & 0 \end{pmatrix}$
Calculation z[001]	$\begin{pmatrix} 0 & 0 & 0 \\ 0 & 0 & 12 \\ 0 & -32 & 0 \end{pmatrix}$	$\begin{pmatrix} 0 & 0 & -12 \\ 0 & 0 & 0 \\ 32 & 0 & 0 \end{pmatrix}$	$\begin{pmatrix} 0 & -1 & 0 \\ 1 & 0 & 0 \\ 0 & 0 & 0 \end{pmatrix}$
Calculation z[112]	$\begin{pmatrix} 0 & 0 & 0 \\ 0 & 10 & 25 \\ 0 & -19 & -10 \end{pmatrix}$	$\begin{pmatrix} 0 & 6 & -3 \\ -15 & 0 & 0 \\ 10 & 0 & 0 \end{pmatrix}$	$\begin{pmatrix} 0 & 8 & -6 \\ -20 & 0 & 0 \\ 16 & 0 & 0 \end{pmatrix}$

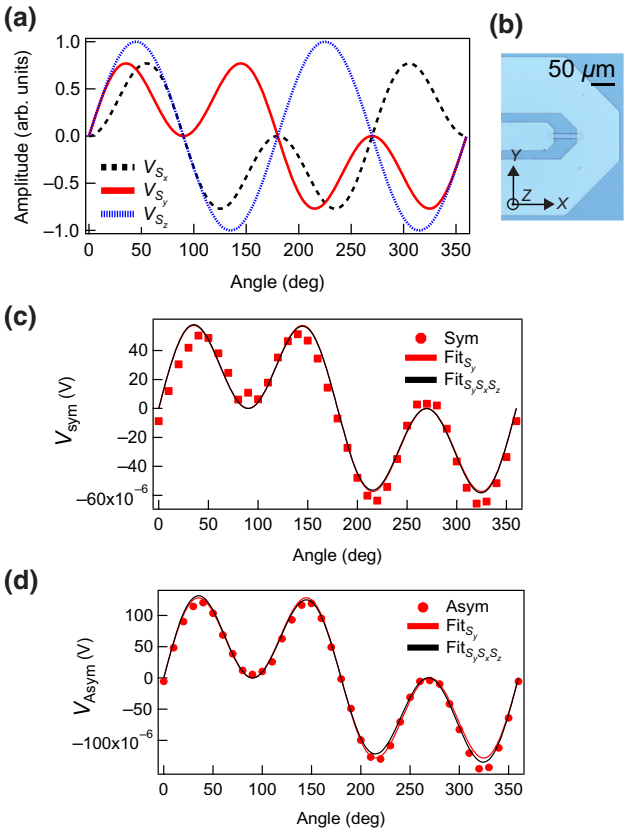

FIG. 6. (a) Theoretical angle dependent functional form of the ST-FMR signal with spin polarization along different axis. (b) Image of one of our samples showing the coordinate axis. Angle dependence of the (b) symmetric and (c) antisymmetric components of the torque fitted with spin polarization along the y axis (red) and all axes (black).

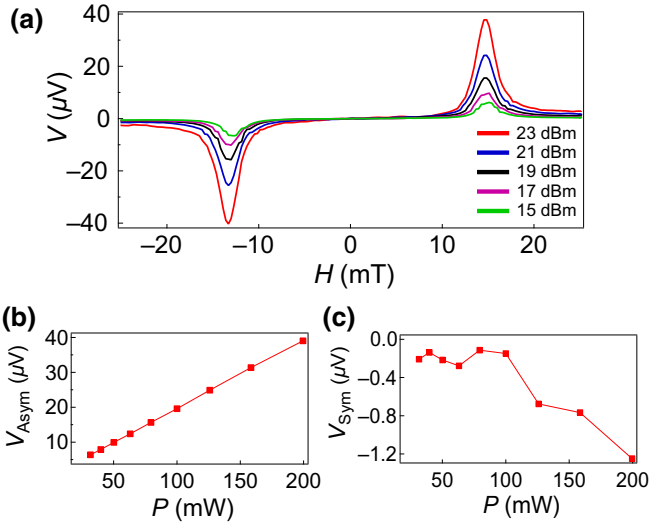

FIG. 7. (a) Voltage signal measured in a Py(30 nm)/Cd_3As_2(40 nm) heterostructure as we sweep the magnetic field. Magnitude of the (b) antisymmetric and (c) symmetric components of the voltage signal at resonance condition as a function of power.

Grant No. DMR-1539916 provided support for ARPES measurements (YO, TP, AR, NS). The magnetometry measurements were carried out by JR, supported by a grant from the University of Chicago. Part of this work was carried out in the College of Science and Engineering Characterization Facility, University of Minnesota, which has received capital equipment funding from the National Science Foundation through the UMN MRSEC under Award Number DMR-2011401 (JH, SG, AM). EG acknowledges support for an undergraduate summer internship from the Office of Graduate Educational Equity Programs and Eberly College of Science at the Pennsylvania State University. B.Y. acknowledges the financial support by the European Research Council (ERC Consolidator Grant No. 815869). Certain commercial equipment, instruments, or materials (or suppliers, or software, etc.) are identified in this paper to foster understanding. Such identification does not imply recommendation or endorsement by the National Institute of Standards and Technology, nor does it imply that the materials or equipment identified are necessarily the best available for the purpose.

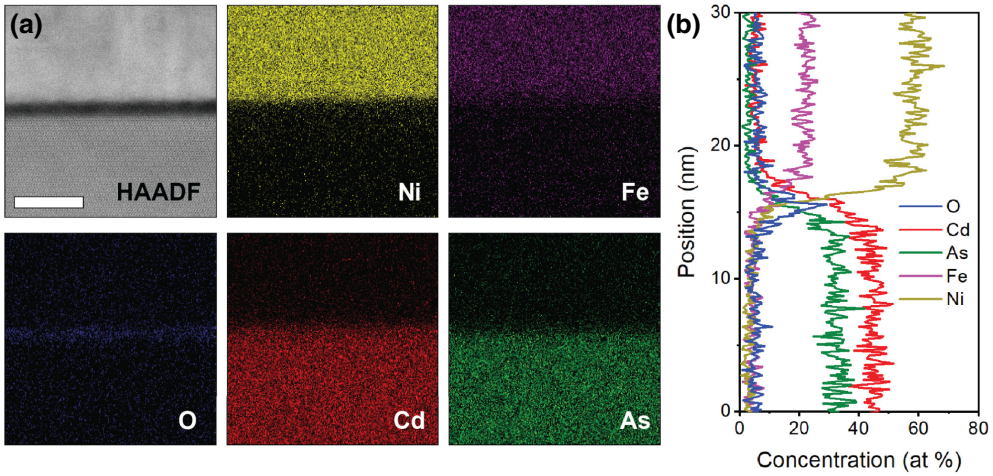

FIG. 8. STEM-EDX elemental map of the Cd_3As_2/Py interface. (a) HAADF-STEM image and elemental maps of Ni, Fe, O, Cd, and As. Scale bar is 10 nm. (b) Concentration of the elements in (a) across the interface. Note the approximately 1 nm amorphous layer of CdO_x at the interface.

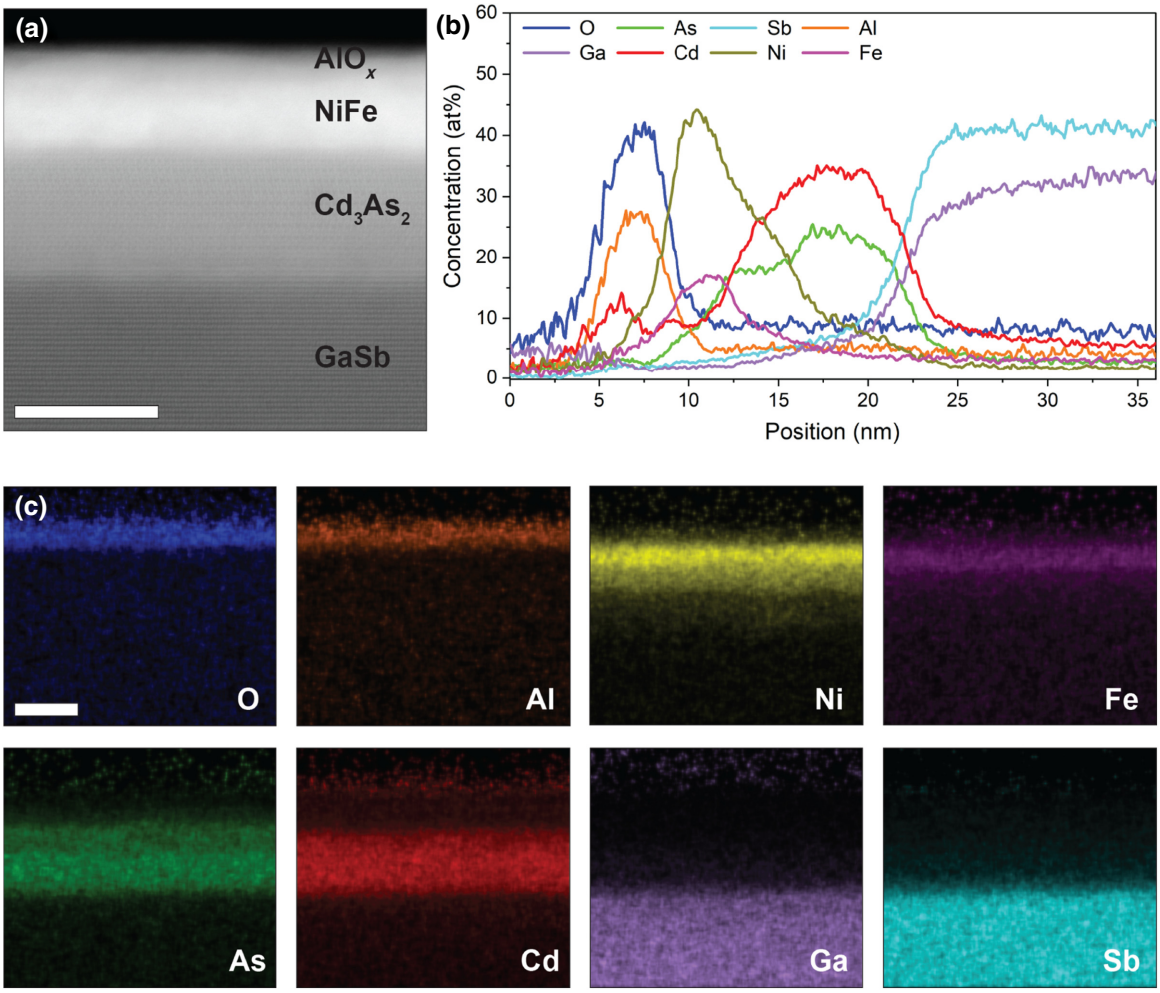

FIG. 9. (a) HAADF-STEM image of the top layers of the device. The scale bar is 10 nm. (b) Concentration of the elements in (a) across the device interface layers shown. (c) Elemental maps of O, Al, Ni, Fe, As, Cd, Ga and Sb. Scale bar is 10 nm.

APPENDIX A: INTRINSIC SPIN HALL EFFECT CALCULATIONS

The spin current J_i^{Sk} generated by electric field $\vec{E}$ via SHC ($J_i^{Sk} = \sigma_{ij}^k E_j$), where J_i^{Sk} flows along i direction when spin polarization along k direction. We evaluate the SHC (σ_{ij}^k) by the Kubo-formula approach in the linear response scheme [36],

$$\sigma_{ij}^k = \frac{e}{\hbar}\sum_n \int_{BZ} \frac{d^3\mathbf{k}}{(2\pi)^3} f_n(\mathbf{k})\Omega_{n,ij}^k(\mathbf{k}), \tag{A1}$$

$$\Omega_{n,ij}^k(\mathbf{k}) = 2i\hbar^2 \sum_{m\neq n} \frac{\langle u_n(\mathbf{k})|\hat{j}_i^k|u_m(\mathbf{k})\rangle\langle u_m(\mathbf{k})|\hat{v}_j|u_n(\mathbf{k})\rangle}{(E_n(\mathbf{k}) - E_m(\mathbf{k}))^2}. \tag{A2}$$

Here, ϵ_n is the eigenvalue of the $|n\rangle$ eigenstate, and $\hat{v}_i = d\hat{H}/\hbar dk_i$ $(i = x, y, z)$ is the velocity operator, f_n is the Fermi-Dirac distribution. Here $\hat{j}_i^j$ is the spin current operator which is related to the velocity operator ($\hat{v}_i$) and spin operator ($\hat{s}_j$) as $\hat{j}_i^j = [\hat{v}_i, \hat{s}_j]$. A k-point of grid of $200 \times 200 \times 200$ is used for the numerical integration in Eq. (A1).

We set the x, y, z axes as the crystallographic a, b, c axes, respectively. According to the space group symmetry and time-reversal symmetry, the σ_{ij}^k tensor has only three independent matrix elements, σ_{xy}^z, σ_{zx}^y, and σ_{yz}^x, as listed in Table I. SHC depends sensitively on the chemical potential, as shown in Fig. 5.

The DFT band structure is shown in Fig. 5. The Dirac point appears at $k_z = \pm k_D$ between Γ and Z, well consistent with previous work. The Dirac bands contribute mainly to the σ_{xy}^z component. This is consistent with the fact that the $k_z = 0$ plane between two Dirac points is a quantum spin Hall insulator. If we approximate all k_z planes between two Dirac points are quantum spin Hall states, then we can estimate the three-dimensional

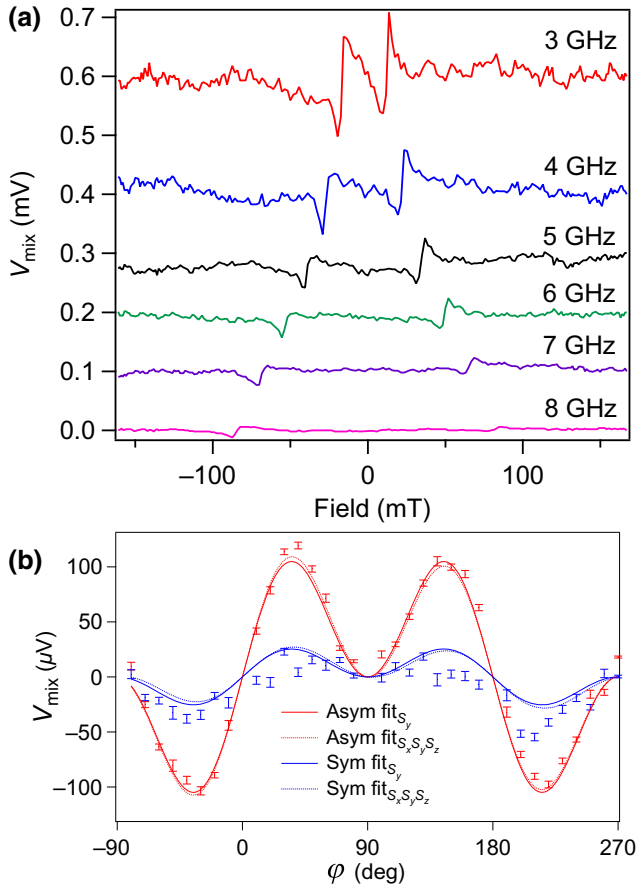

FIG. 10. (a) ST-FMR mixing voltage measured at different frequencies in a completely *in vacuo* grown heterostructure. (b) Angle dependance of the symmetric (red) and antisymmetric (blue) components of the torque fitted with an in plane spin polarization (continuous line) and a three-dimensional spin polarization (dotted line).

SHC by

$$\sigma_{xy}^{z} = \frac{k_D}{k_Z}\left(\frac{1}{c/2}\right)\frac{2e^2}{h}\left(\frac{\hbar/2}{e}\right), \tag{A3}$$

where k_Z is the Γ–Z distance in the Brillouin zone, $2e^2/h$ is the conductance quantum, c is the lattice parameter of the tetragonal unitcell, and $\hbar/(2e)$ converts the dimension from the charge current to the spin current. By taking $k_D/k_Z = 14\%$ from the band structure and lattice parameter $c = 25.4$ Å, we obtain $\sigma_{xy}^{z} \approx 40\ \mathrm{S\,cm^{-1}}$ $(\hbar/e)$. This is actually very close to the numerical value in Table I.

When rotating the z axis to the [112] crystallographic axis, which is approximately the [111] direction in the Cartesian's coordinate. We can transform the SHC tensor by the unitary rotation [55],

$$\sigma_{[112]_{ij}}^{k} = \sum_{l,m,n} D_{il}D_{jm}D_{kn}\sigma_{[001]_{lm}}^{n}, \tag{A4}$$

where D_{lm} is the rotation matrix element that rotates the z axis to the [112] crystallographic axis. The transformed SHC matrix is listed in Table I and II.

When x, y align in the (112) crystallographic plane, the new x, y, z axes are not high-symmetry lines as those before. Therefore, new matrix elements emerge in the SHC. When charge flows in the x, y plane and spin flows along z as the experiment setup, $\sigma_{zx}^{y}, \sigma_{zx}^{z}, \sigma_{zy}^{x}$ are the relevant SHC matrix elements. Here, $\sigma_{zx}^{y} = 10\ \mathrm{S\,cm^{-1}}$ $(\hbar/e)$ is about one order of magnitude smaller than the experimental SHC, $140\ \mathrm{S\,cm^{-1}}$ $(\hbar/e)$. This suggests that the main contributions to the observed SHE are related to extrinsic effects. In addition, σ_{zx}^{z} indicates the existence of an out-of-plane spin component in the spin current. Suppose the intrinsic SHE prevails under certain experimental conditions, we expect that the out-of-plane polarization may play a significant role in the spin-orbit torque.

APPENDIX B: ANALYSIS OF SPIN POLARIZATION IN ST-FMR MEASUREMENTS

Following the procedure sketched in [41], we can study the direction of the spin polarization of the spin current in Cd_3As_2 by performing an angle-dependent ST-FMR measurement. Different polarizations will contribute to different functional forms of the spin current [Fig. 6(a)]:

$$V_{S_x} \propto \sin(\phi)\sin(2\phi), \quad V_{S_y} \propto \cos(\phi)\sin(2\phi),$$
$$V_{S_z} \propto \sin(2\phi). \tag{B1}$$

We fit the symmetric and antisymmetric ST-FMR data with a spin polarization along the y axis and along all three axes [Figs. 6(c) and 6(d)]. The two fits do not show any significant differences. In the latter case, the amplitudes of the voltage signal with spin polarization along the x and z axis (V_{S_x} and V_{S_z}) are less than 5% the value with spin polarization along the y axis (V_{S_y}). Thus, we are confident that the direction of the spin polarization of the measured torque is in the plane of the sample and transverse to the current direction.

APPENDIX C: SYMMETRIC AND ANTISYMMETRIC COMPONENTS OF THE SPIN PUMPING SIGNAL

As mentioned in the main text, the voltage signal measured in our samples [Fig. 7(a)] can be decomposed in an antisymmetric signal that changes sign under field reversal [V_{asym} shown in Fig. 7(b)] and a symmetric signal that does not [V_{sym} shown in Fig. 7(c)]. When we increased the power in the transmission line, we found that V_{asym} increases linearly as expected from ferromagnetic driven spin pumping into the Cd_3As_2 layer from the NiFe ferromagnet. The symmetric signal has an amplitude of less than 4% of the asymmetric signal and is nonlinear with

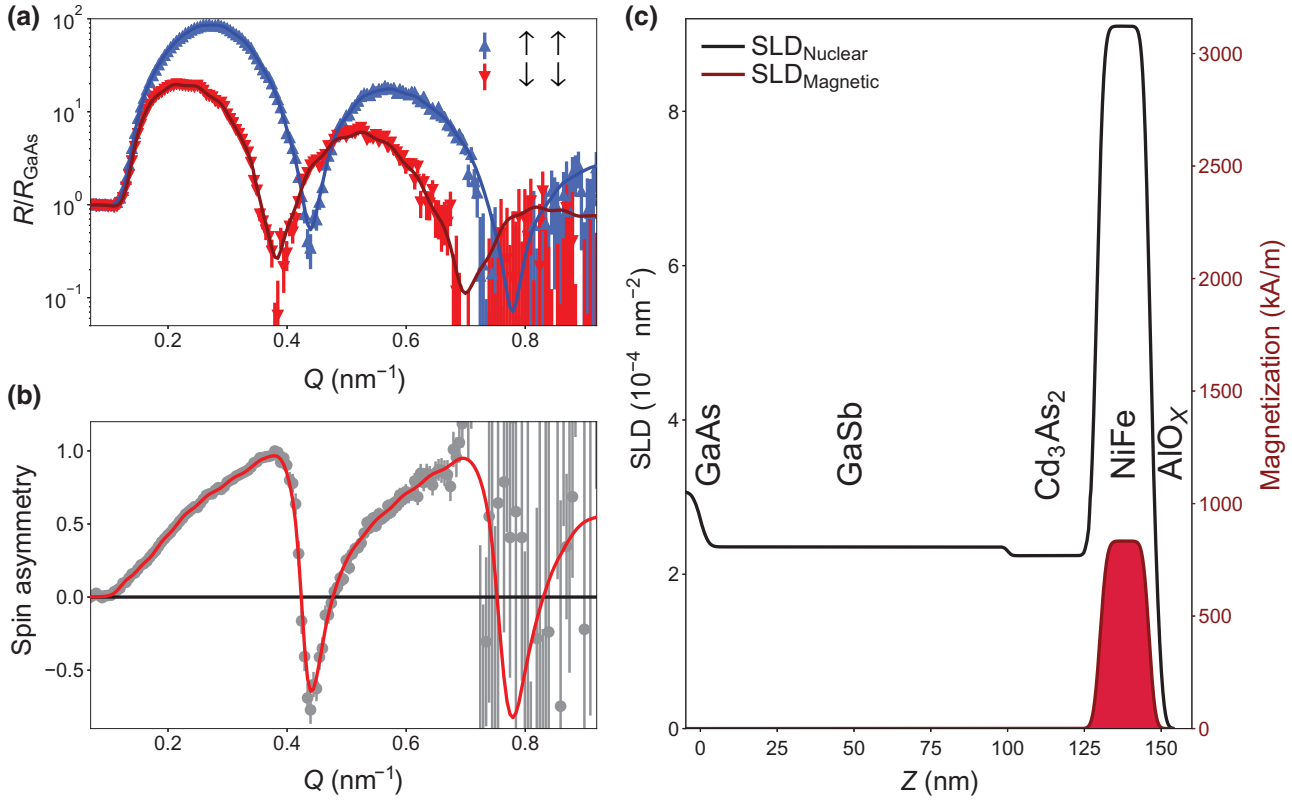

FIG. 11. (a) Spin-dependent PNR data from a Cd_3As_2/Py bilayer at room temperature in an applied field of 2 T alongside a theoretical fit. We show the Fresnel reflectivity, where the measured reflectivity is normalized by the Q-dependent theoretical reflectivity of the GaAs substrate. (b) Measured spin asymmetry, defined as $(R^{\uparrow\uparrow} - R^{\downarrow\downarrow})/(R^{\uparrow\uparrow} + R^{\downarrow\downarrow})$ alongside theoretical fit. (c) Best fit nuclear and magnetic scattering length density (SLD) profiles used to generate the fits shown. The right axis shows the magnetization which is equivalent to a given magnetic SLD value.

power. This is consistent with a possible Seebeck effect induced by the microstrip not being perfectly centered over the sample [43].

APPENDIX D: STUDY OF THE Cd_3As_2/Py INTERFACE

In the samples presented in the main text, atomic resolution HAADF STEM and EDX spectroscopy of the Cd_3As_2/Py heterostructures show a 1–1.5 nm thick amorphous CdO_x layer at the interface (Fig. 8). This probably forms during the ambient condition transfer of samples from the MBE chamber to the metal evaporation chamber.

To avoid the oxidation effect at the Cd_3As_2/Py interface, we have fabricated ST-FMR devices using a full in vacuum transfer procedure with a vacuum suitcase. Differences in sample holder configurations that allowed the compatibility between chambers seemed to increase the roughness of the Cd_3As_2 layer which increased the noise level in our measurements. Nevertheless as seen in Fig. 9, we have successfully been able to remove the oxide layer at the interface. Moreover, we have been able to measure an ST-FMR signal that clearly shows resonance up to 8 GHz (Fig. 10). This allowed us to compute the spin torque efficiency $\xi = 0.10$ and SHC $\sigma_{SH} \gtrsim 63(\hbar/e)$ S cm of this device. This experimental value is closer to the intrinsic theoretical one and seems to indicate the possibility that the CdO_x layer enhances the extrinsic spin Hall effect. Furthermore, the data corroborate that the measured signal is due to charge to spin conversion in the Cd_3As_2/Py interface as presented in the main text.

APPENDIX E: PNR MEASUREMENTS IN Cd_3As_2/Py HETEROSTRUCTURES

To examine the possibility of proximity-induced magnetism in the Cd_3As_2 layer caused by the adjacent ferromagnetic Py layer, we performed room-temperature PNR measurements at the PBR instrument at the NIST Center for Neutron Research (NCNR). The incident neutrons ($\lambda = 4.75$ A^{-1}) were spin polarized parallel or antiparallel to the 2 T applied in-plane magnetic field, and the specular reflectivity was measured as a function of Q, the momentum transfer vector along the film normal direction. The spin-dependent neutron reflectivity is sensitive to the nuclear and magnetic scattering length density (SLD) depth profiles, so that depth-resolved information on the

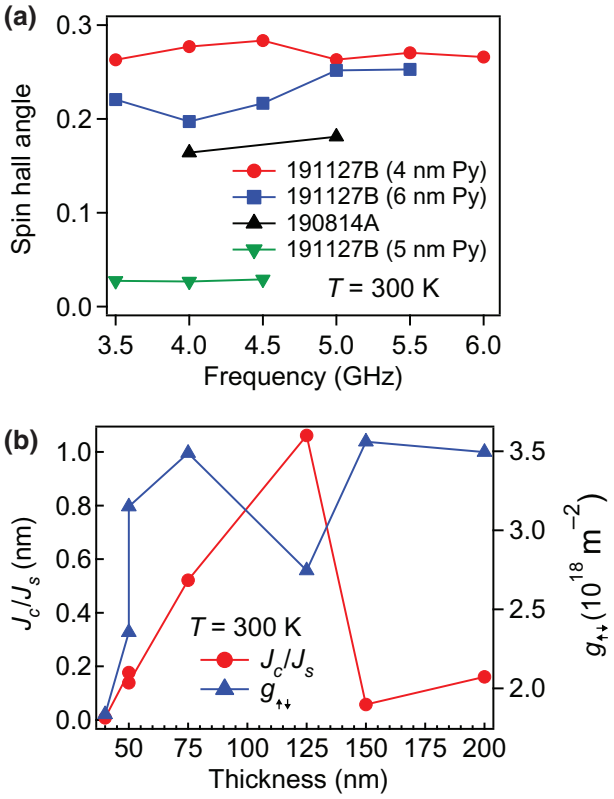

FIG. 12. (a) Spin Hall angle determined from ST-FMR at different frequencies in different samples. (b) The J_c/J_s ratio and spin mixing conductance ($g_{\uparrow\downarrow}$) obtained from SP in heterostructures with 30 nm of NiFe and variable Cd_3As_2 thickness.

structure and magnetization may be extracted through fitting. As the 2 T in-plane field is more than sufficient to saturate the Py magnetization, no in-plane component of the magnetization is expected to be perpendicular to the applied field. Therefore, only the nonspin flip reflectivity cross sections, sensitive to the in-plane magnetization parallel to the applied field, were collected while the spin-flip cross sections, sensitive only to the in-plane magnetization perpendicular to the applied field, were not. We reduced and analyzed the data using the Reductus and Refl1D software programs, respectively [56,57]. Parameter uncertainties were estimated using a Markov chain Monte Carlo (MCMC) method as implemented in the DREAM algorithm of the BUMPS PYTHON package.

The best fit to the data, shown in Fig. 11, was generated using a model which allowed for a proximity-induced magnetization of varying thickness in the Cd_3As_2 at the interface with the Py layer. However, the best fit to the data yields no induced magnetization in the Cd_3As_2 at the interface, indicating a lack of proximity-induced magnetization within measurement sensitivity. As the thickness and magnetization of a proximity-magnetized layer are often highly coupled parameters, uncertainty analysis was performed using a modified model in which the proximity-magnetized layer thickness was fixed at a typical value of 2 nm. In this case, DREAM analysis indicates an extremely small upper limit (95% confidence interval) of 10 kA/m. The model shown does not incorporate the CdO_x layer observed in STEM imaging, as modeling which incorporated this layer did not yield a notably different fit from those that did not. This will be understood given that the extremely thin 1 nm layer yields oscillations with a periodicity of approximately 6.28 nm^{-1} in Q, far outside the measured range. Further, the expected CdO_x thickness is the same order of magnitude as the fitted roughness at the Cd_3As_2/Py interface. Lastly, we note that the theoretical nuclear SLD (4.065×10^{-4} nm^{-2}) of CdO_x is between that of Cd_3As_2 and Py. Taken together, these factors suggest that the structural features associated with the CdO_x layer are likely to be extremely muted. Rather, we propose that the CdO_x layer will blend into the Cd_3As_2 interface and will likely instead manifest in the SLD profile as a small magnetically dead layer in the Py at the Cd_3As_2 interface. Indeed, incorporating such a magnetically dead layer in Py near the Cd_3As_2 interface into the model yields a thickness of 1.04 nm $\pm$ 0.07 nm, in excellent agreement with the STEM and EELS. PNR measurements therefore indicate a lack of proximity-induced magnetization at room temperature and confirm the presence of a nonmagnetic oxide-like layer at the interface.

TABLE III. Samples used in this study indicating the nominal thickness of the Cd_3As_2 and Py layers and the measurement performed to study the spin-charge interconversion. Samples with an * were used to calibrate the deposition rate via transmission electron microscopy (TEM) and X-ray reflectivity (XRR).

Sample number	Cd_3As_2 thickness (nm)	NiFe thickness (nm)	Measurement performed
190130A	40	30	SP
190509A*	50	30	SP, TEM, XRR
190510A*	125	30	SP, TEM, XRR
190612A	50	30	SP
190703A	75	30	SP
190718A	150	30	SP
190719A	200	30	SP
190814A	80	4	ST-FMR
190929A	20	4	ST-FMR,
191002B*	19	4	ST-FMR, XRR
191127B*	12	4, 5, 6	SP, ST-FMR, XRR
201125A*	8	7	ST-FMR, TEM

APPENDIX F: SUMMARY OF THE SAMPLES MEASURED IN THIS STUDY

As mentioned in the main text, we have measured spin and charge interconversion in 13 devices. In Fig. 12 we show the spin Hall angle and J_c/J_s ratio for the ST-FMR

and SP samples used in this study. Furthermore, Table III lists the thickness of the NiFe and Cd_3As_2 layers in each heterostructure and the measurements performed.

[1] O. Mosendz, V. Vlaminck, J. E. Pearson, F. Y. Fradin, G. E. W. Bauer, S. D. Bader, and A. Hoffmann, Detection and quantification of inverse spin Hall effect from spin pumping in permalloy/normal metal bilayers, Phys. Rev. B **82**, 214403 (2010).

[2] V. Vlaminck, J. E. Pearson, S. D. Bader, and A. Hoffmann, Dependence of spin-pumping spin Hall effect measurements on layer thicknesses and stacking order, Phys. Rev. B **88**, 064414 (2013).

[3] I. Mihai Miron, G. Gaudin, S. Auffret, B. Rodmacq, A. Schuhl, S. Pizzini, J. Vogel, and P. Gambardella, Current-driven spin torque induced by the Rashba effect in a ferromagnetic metal layer, Nat. Mater. **9**, 230 (2010).

[4] L. Liu, C.-F. Pai, Y. Li, H. W. Tseng, D. C. Ralph, and R. A. Buhrman, Spin-torque switching with the giant spin Hall effect of tantalum, Science **336**, 555 (2012).

[5] Y. Ou, D. C. Ralph, and R. A. Buhrman, Strong Enhancement of the Spin Hall Effect by Spin Fluctuations near the Curie Point of Fe_xPt_{1-x} Alloys, Phys. Rev. Lett. **120**, 097203 (2018).

[6] A. Hoffmann, Spin Hall effects in metals, IEEE Trans. Magn. **49**, 5172 (2013).

[7] C.-F. Pai, L. Liu, Y. Li, H. W. Tseng, D. C. Ralph, and R. A. Buhrman, Spin transfer torque devices utilizing the giant spin Hall effect of tungsten, Appl. Phys. Lett. **101**, 122404 (2012).

[8] H. Wang, J. Kally, J. S. Lee, T. Liu, H. Chang, D. R. Hickey, K. A. Mkhoyan, M. Wu, A. Richardella, and N. Samarth, Surface-State-Dominated Spin-Charge Current Conversion in Topological-Insulator–Ferromagnetic-Insulator Heterostructures, Phys. Rev. Lett. **117**, 076601 (2016).

[9] H. Wang, J. Kally, C. Şahin, T. Liu, W. Yanez, E. J. Kamp, A. Richardella, M. Wu, M. E. Flatté, and N. Samarth, Fermi level dependent spin pumping from a magnetic insulator into a topological insulator, Phys. Rev. Res. **1**, 012014(R) (2019).

[10] A. R. Mellnik, J. S. Lee, A. Richardella, J. L. Grab, P. J. Mintun, M. H. Fischer, A. Vaezi, A. Manchon, E.-A. Kim, N. Samarth, and D. C. Ralph, Spin-transfer torque generated by a topological insulator, Nature **511**, 449 (2014).

[11] K. Kondou, R. Yoshimi, A. Tsukazaki, Y. Fukuma, J. Matsuno, K. S. Takahashi, M. Kawasaki, Y. Tokura, and Y. Otani, Fermi-level-dependent charge-to-spin current conversion by Dirac surface states of topological insulators, Nat. Phys. **12**, 1027 (2016).

[12] Y. Wang, R. Ramaswamy, and H. Yang, FMR-related phenomena in spintronic devices, J. Phys. D: Appl. Phys. **51**, 273002 (2018).

[13] Y. Sun, Y. Zhang, C. Felser, and B. Yan, Strong Intrinsic Spin Hall Effect in the TaAs Family of Weyl Semimetals, Phys. Rev. Lett. **117**, 146403 (2016).

[14] A. Johansson, J. Henk, and I. Mertig, Edelstein effect in Weyl semimetals, Phys. Rev. B **97**, 085417 (2018).

[15] S. S.-L. Zhang, A. A. Burkov, I. Martin, and O. G. Heinonen, Spin-To-Charge Conversion in Magnetic Weyl Semimetals, Phys. Rev. Lett. **123**, 187201 (2019).

[16] D. MacNeill, G. M. Stiehl, M. H. D. Guimaraes, R. A. Buhrman, J. Park, and D. C. Ralph, Control of spin-orbit torques through crystal symmetry in WTe_2/ferromagnet bilayers, Nat. Phys. **13**, 300 (2016).

[17] D. MacNeill, G. M. Stiehl, M. H. D. Guimarães, N. D. Reynolds, R. A. Buhrman, and D. C. Ralph, Thickness dependence of spin-orbit torques generated by WTe_2, Phys. Rev. B **96**, 054450 (2017).

[18] S. Shi, S. Liang, Z. Zhu, K. Cai, S. D. Pollard, Y. Wang, J. Wang, Q. Wang, P. He, J. Yu, G. Eda, G. Liang, and H. Yang, All-electric magnetization switching and Dzyaloshinskii-Moriya interaction in WTe2/ferromagnet heterostructures, Nat. Nanotechnol. **14**, 945 (2019).

[19] B.-C. Lin, S. Wang, A.-Q. Wang, Y. Li, R.-R. Li, K. Xia, D. Yu, and Z.-M. Liao, Electric Control of Fermi Arc Spin Transport in Individual Topological Semimetal Nanowires, Phys. Rev. Lett. **124**, 116802 (2020).

[20] A.-Q. Wang, P.-Z. Xiang, X.-G. Ye, W.-Z. Zheng, D. Yu, and Z.-M. Liao, Room-Temperature Manipulation of Spin Texture in a Dirac Semimetal, Phys. Rev. Appl. **14**, 054044 (2020).

[21] H. Xu, J. Wei, H. Zhou, J. Feng, T. Xu, H. Du, C. He, Y. Huang, J. Zhang, Y. Liu, H.-C. Wu, C. Guo, X. Wang, Y. Guang, H. Wei, Y. Peng, W. Jiang, G. Yu, and X. Han, High spin Hall conductivity in large-area type-II dirac semimetal $PtTe_2$, Adv. Mater. **32**, 2000513 (2020).

[22] G. M. Stephen, A. T. Hanbicki, T. Schumann, J. T. Robinson, M. Goyal, S. Stemmer, and A. L. Friedman, Room-temperature spin transport in Cd_3As_2, ACS Nano **15**, 5459 (2021).

[23] S.-Y. Xu, C. Liu, S. K. Kushwaha, R. Sankar, J. W. Krizan, I. Belopolski, M. Neupan, G. Bian, N. Alidoust, T.-R. Chang, H.-T. Jeng, C.-Y. Huang, W.-F. Tsai, H. Lin, P. P. Shibayev, F. Chou, R. J. Cava, and M. Z. Hasan, Observation of Fermi arc surface states in a topological metal, Science **347**, 294 (2015).

[24] S. Shi, Y. Ou, S. V. Aradhya, D. C. Ralph, and R. A. Buhrman, Fast Low-Current Spin-Orbit-Torque Switching of Magnetic Tunnel Junctions through Atomic Modifications of the Free-Layer Interfaces, Phys. Rev. Appl. **9**, 011002(R) (2018).

[25] S. Fukami and H. Ohno, Magnetization switching schemes for nanoscale three-terminal spintronics devices, JJAP **56**, 0802A1 (2017).

[26] T. Schumann, M. Goyal, H. Kim, and S. Stemmer, Molecular beam epitaxy of Cd_3As_2 on a III–V substrate, APL Mater. **4**, 126110 (2016).

[27] Z. K. Liu, J. Jiang, B. Zhou, Z. J. Wang, Y. Zhang, H. M. Weng, D. Prabhakaran, S.-K. Mo, H. Peng, P. Dudin, T. Kim, M. Hoesch, Z. Fang, X. Dai, Z. X. Shen, D. L. Feng, Z. Hussain, and Y. L. Chen, A stable three-dimensional topological Dirac semimetal Cd_3As_2, Nat. Mater. **13**, 677 (2014).

[28] S. Borisenko, Q. Gibson, D. Evtushinsky, V. Zabolotnyy, B. Büchner, and R. J. Cava, Experimental Realization of a Three-Dimensional Dirac Semimetal, Phys. Rev. Lett. **113**, 027603 (2014).

[29] H. Yi, *et al.*, Evidence of topological surface state in three-dimensional dirac semimetal Cd_3As_2, Sci. Rep. **4**, 6106 (2014).
[30] Y. Liu, C. Zhang, X. Yuan, T. Lei, C. Wang, D. Di Sante, A. Narayan, L. He, S. Picozzi, S. Sanvito, R. Che, and F. Xiu, Gate-tunable quantum oscillations in ambipolar Cd_3As_2 thin films, NPG Asia Mater. **7**, e221 (2015).
[31] P. Cheng, C. Zhang, Y. Liu, X. Yuan, F. Song, Q. Sun, P. Zhou, D. W. Zhang, and F. Xiu, Thickness-dependent quantum oscillations in Cd_3As_2 thin films, New J. Phys. **18**, 083003 (2016).
[32] C.-Z. Li, J.-G. Li, L.-X. Wang, L. Zhang, J.-M. Zhang, D. Yu, and Z.-M. Liao, Two-carrier transport induced Hall anomaly and large tunable magnetoresistance in Dirac semimetal Cd_3As_2 nanoplates, ACS Nano **10**, 6020 (2016).
[33] J. P. Perdew, K. Burke, and M. Ernzerhof, Generalized Gradient Approximation Made Simple, Phys. Rev. Lett. **77**, 3865 (1996).
[34] K. Koepernik and H. Eschrig, Full-potential nonorthogonal local-orbital minimum-basis band-structure scheme, Phys. Rev. B **59**, 1743 (1999).
[35] M. N. Ali, Q. Gibson, S. Jeon, B. B. Zhou, A. Yazdani, and R. J. Cava, The crystal and electronic structures of Cd_3As_2, the three-dimensional electronic analogue of graphene, Inorg. Chem. **53**, 4062 (2014).
[36] J. Sinova, S. O. Valenzuela, J. Wunderlich, C. H. Back, and T. Jungwirth, Spin Hall effects, Rev. Mod. Phys. **87**, 1213 (2015).
[37] E. Lesne, Y. Fu, S. Oyarzun, J. C. Rojas-Sánchez, D. C. Vaz, H. Naganuma, G. Sicoli, J.-P. Attané, M. Jamet, E. Jacquet, J.-M. George, A. Barthélémy, H. Jaffrès, A. Fert, M. Bibes, and L. Vila, Highly efficient and tunable spin-to-charge conversion through Rashba coupling at oxide interfaces, Nat. Mater. **15**, 1261 (2016).
[38] L. Liu, T. Moriyama, D. C. Ralph, and R. A. Buhrman, Spin-Torque Ferromagnetic Resonance Induced by the Spin Hall Effect, Phys. Rev. Lett. **106**, 036601 (2011).
[39] C.-F. Pai, Y. Ou, L. H. Vilela-Leão, D. C. Ralph, and R. A. Buhrman, Dependence of the efficiency of spin Hall torque on the transparency of Pt/ferromagnetic layer interfaces, Phys. Rev. B **92**, 064426 (2015).
[40] Y. Ou, C.-F. Pai, S. Shi, D. C. Ralph, and R. A. Buhrman, Origin of fieldlike spin-orbit torques in heavy metal/ferromagnet/oxide thin film heterostructures, Phys. Rev. B **94**, 140414(R) (2016).
[41] Y. Ou, Z. Wang, C. S. Chang, H. P. Nair, H. Paik, N. Reynolds, D. C. Ralph, D. A. Muller, D. G. Schlom, and R. A. Buhrman, Exceptionally high, strongly temperature dependent, spin Hall conductivity of $SrRuO_3$, Nano Lett. **19**, 3663 (2019).
[42] M. Jamali, J. S. Lee, J. S. Jeong, F. Mahfouzi, Y. Lv, Z. Zhao, B. K. Nikolic, K. A. Mkhoyan, N. Samarth, and J.-P. Wang, Giant spin pumping and inverse spin Hall effect in the presence of surface and bulk spin-orbit coupling of topological insulator Bi_2Se_3, Nano Lett. **15**, 7126 (2015).
[43] Y. Shiomi, K. Nomura, Y. Kajiwara, K. Eto, M. Novak, K. Segawa, Y. Ando, and E. Saitoh, Spin-Electricity Conversion Induced by Spin Injection Into Topological Insulators, Phys. Rev. Lett. **113**, 196601 (2014).
[44] Y. Tserkovnyak, A. Brataas, and G. E. W. Bauer, Enhanced Gilbert Damping in Thin Ferromagnetic Films, Phys. Rev. Lett. **88**, 117601 (2002).
[45] R. M. Stroud, A. T. Hanbicki, Y. D. Park, G. Kioseoglou, A. G. Petukhov, B. T. Jonker, G. Itskos, and A. Petrou, Reduction of Spin Injection Efficiency by Interface Defect Spin Scattering in ZnMnSe/AlGaAs–GaAs Spin-Polarized Light-Emitting Diodes, Phys. Rev. Lett. **89**, 166602 (2002).
[46] Z. Qiu, D. Hou, K. Uchida, and E. Saitoh, Influence of interface condition on spin-Seebeck effects, J. Phys. D: Appl. Phys. **48**, 164013 (2015).
[47] J. Fontcuberta, H. B. Vasili, J. Gàzquez, and F. Casanova, On the role of interfaces on spin transport in magnetic insulator/normal metal heterostructures, Adv. Mater. Interfaces **6**, 1900475 (2019).
[48] H. An, Y. Kageyama, Y. Kanno, N. Enishi, and K. Ando, Spin–torque generator engineered by natural oxidation of Cu, Nat. Commun. **7**, 13069 (2016).
[49] H. Tsai, S. Karube, K. Kondou, N. Yamaguchi, F. Ishii, and Y. Otani, Clear variation of spin splitting by changing electron distribution at non-magnetic metal/Bi_2O_3 interfaces, Sci. Rep. **8**, 5564 (2018).
[50] D. Go, D. Jo, T. Gao, K. Ando, S. Blügel, H.-W. Lee, and Y. Mokrousov, Orbital Rashba effect in a surface-oxidized Cu film, Phys. Rev. B **103**, L121113 (2021).
[51] Y. Kageyama, Y. Tazaki, H. An, T. Harumoto, T. Gao, J. Shi, and K. Ando, Spin-orbit torque manipulated by fine-tuning of oxygen-induced orbital hybridization, Sci. Adv. **5**, eaax4278 (2019).
[52] L. Yang, Y. Fei, K. Zhou, L. Chen, Q. Fu, L. Li, C. Yan, H. Li, Y. Du, and R. Liu, Maximizing spin-orbit torque efficiency of Ta(O)/Py via modulating oxygen-induced interface orbital hybridization, Appl. Phys. Lett. **118**, 032405 (2021).
[53] S. Haku, A. Musha, T. Gao, and K. Ando, Role of interfacial oxidation in the generation of spin-orbit torques, Phys. Rev. B **102**, 024405 (2020).
[54] S. Karube, D. Sugawara, C. Tang, T. Tanabe, Y. Oyama, and J. Nitta, Enhancement of spin-charge current interconversion by oxidation of rhenium, J. Magn. Magn. Mater. **516**, 167298 (2020).
[55] M. Seemann, D. Kodderitzsch, S. Wimmer, and H. Ebert, Symmetry-imposed shape of linear response tensors, Phys. Rev. B **92**, 155138 (2015).
[56] B. Maranville, W. Ratcliff, and P. Kienzle, Reductus: A stateless Python data-reduction service with a browser frontend, J. Appl. Cryst. **51**, 1500 (2018).
[57] B. Kirby, P. Kienzle, B. Maranville, N. Berk, J. Krycka, F. Heinrich, and C. Majkrzak, Phase-sensitive specular neutron reflectometry for imaging the nanometer scale composition depth profile of thin-film materials, Curr. Opin. Colloid Interface Sci. **17**, 44 (2012).